Electronic Supplementary Material (ESI) for Journal of Materials Chemistry A.
This journal is © The Royal Society of Chemistry 2019

COMPARISONS OF WO_3 REDUCTION TO H_XWO_3 UNDER THERMOCHEMICAL AND ELECTROCHEMICAL CONTROL

SUPPLEMENTARY INFORMATION

Evan V. Miu
Department of Chemical and Petroleum Engineering
University of Pittsburgh
Pittsburgh, PA 15261

James R. McKone
Department of Chemical and Petroleum Engineering
University of Pittsburgh
Pittsburgh, PA 15261
jmckone@pitt.edu

1 Detailed Experimental Methods

The WO_3 nanodisks used in this study were prepared using a method adapted from Wolcott et al.[1] In a representative synthesis, 0.8225 grams of Na_2WO_4 hydrate (Sigma Aldrich, $\geq 99\%$) was dissolved in 10 mL of deionized water (>18 MΩ, Millipore Advantage A-10) to form a 0.25 M solution. A liquid chromatography column wth a 1.5 cm ID was packed with 5 cm of hydrogen-form Dowex 50WX8 ion exchange resin (200–400 mesh, Sigma Aldrich) and washed with water to remove any remaining free acid. A 1 cm layer of sand was packed on top of the resin to ensure even propagation of solution through the column. The 10 mL of Na_2WO_4 solution was then passed through the column in three approximately equal aliquots and collected. The first aliquot was discarded and only the second and third were used in experiments. The exchanged material (nominally 0.25 M tungstic acid) was allowed to rest on the benchtop at room temperature (~21° C) for at least 3 days, whereupon the material geometry was found to converge to a nanodisk morphology. Nanodisk formation was further investigated via SEM, XRD, and TEM, as shown in the main text and Section 2 below.

The aged WO_3 was deposited without any further processing via a doctor-blade method onto glass substrates that had been pre-coated with either FTO, metal thin films, or Pt/WO_3 films. FTO glass was purchased from MTI Corp., where metal thin films and Pt/WO_3 films were applied in-house (see below). The deposition areas were outlined with a single layer of 3M brand Scotch tape and 50 μL of tungstic acid were placed in the center of the boundary. A flint glass tube was used to form an even coat and remove excess material, after which a Steinel HL 1610 S heat gun on the low setting was used to dry the wet films. After drying, the tape was removed and the samples were calcined at 500 °C for one hour in air. Pure WO_3 nanodisk films were allowed to overlap with the pre-deposited metal or Pt/WO_3 films. This overlap region allowed for electrical and chemical interaction between the different materials.

Pt- and Au-coated substrates were prepared using a Plassys MEB550S Electron Beam Evaporator. All depositions were performed at pressures lower than 1E-6 mbar. Corning 75 x 25 mm glass microscope slides were masked using single-sided Kapton tape and initially coated with a 5 nm titanium adhesion layer at a rate of 0.02 nm/sec. A 100 nm layer of either Pt or Au was then deposited onto the Ti-coated glass at respective rates of 0.1 nm/sec and 0.05 nm/sec.

Powder X-ray diffraction (XRD) measurements were performed on a Bruker D-8 instrument equipped with a LynxEye detector and using Cu K-α radiation with a wavelength of 0.15406 Å. Measurements were made with a step size of 0.02° at 1.25 s/step. Scanning electron microscope (SEM) images were taken using a Zeiss Sigma 500VP field emission instrument. Samples were prepared on FTO glass and images were captured using accelerating voltages of 10 keV using a backscatter (SE2) detector. Transmission electron microscopy (TEM) was performed using a Hitachi 9500 ETEM at an accelerating voltage of 300 keV. Samples were dispersed onto dual-sided copper-carbon TEM grids from Ted Pella, Inc. using a 4:1 mixture of IPA:water.

Electrochemical measurements were carried out using a Gamry Interface 1000 potentiostat in a 3-electrode configuration with graphite rod counter and 1 M KCl Ag/AgCl reference electrodes. Samples were tested an acrylic cell that was fabricated in-house, with a 0.495 cm^2 working area. The RHE potential was explicitly calibrated for the 1 M KCl Ag/AgCl reference electrode via open circuit potential (OCP) measurements in a cell consisting of a Pt working electrode, a graphite counter electrode, and 0.5 M sulfuric acid electrolyte.

Time-resolved optical microscopy measurements were carried out on a Pace Technologies IM-5000 Inverted Microscope mounted with a Sony a6300 digital camera. Figure S1 shows the electrochemical configuration of the experimental setup employed for these measurements. The same acrylic cell was used for H-spillover measurements. The sampling area of a

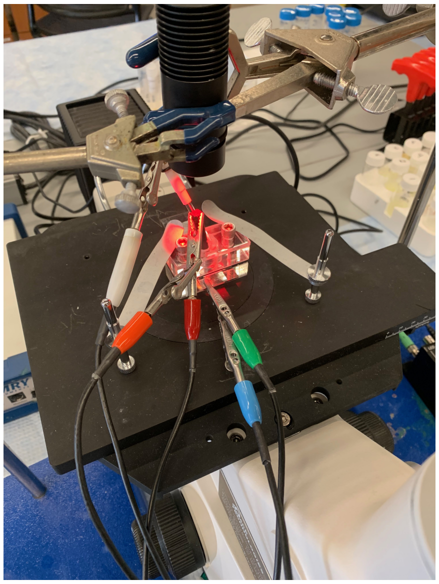

Figure S1: Experimental setup for optical microscopy, shown in the configuration for electrochemical hydrogen insertion with red LED illumination. Camera mounted to microscope not shown.

given video recording was a 3 mm diameter circle, which limited the measurable coloration distance. Both ambient light and a Thorlabs M625L3 625 nm red LED were used as light sources, which gave comparable results. Electrochemical intercalation or thermochemical spillover was instigated at one end of a film, respectively by chronoamperometry or by exposure to hydrogen gas-saturated 0.5 M sulfuric acid. As the respective reductions were induced, WO_3 was progressively converted to its bronze. The conversion from oxide to bronze progressed parallel to the film, evidenced by a coloration front originating at the bias location and extending outwards.

Front progression was explicitly measured only in areas of pure WO_3/H_xWO_3 directly on glass. Videos were recorded at a resolution of 1920 x 1080 and a framerate of 60 fps while either electrochemical (chronoamperometric) or thermochemical (H_2-saturated water) experiments were carried out. A Python script using the `ffmpeg` and `scikit-image` packages was used to convert the raw video file into a series of images with timestamps. Raw pixel-by-pixel intensity data were then collected from each image and converted from RGB color channels to a single gray color channel using the `scikit-image` package's `rgb2gray` function. This converted the multi-channel information to a single-valued pixel intensity. These intensity data were then interpreted as relative transmittance values under the assumption that pixel intensities were linearly proportional to the number of transmitted photons. The resulting data were then converted to relative absorbances by referencing the transmittance at each timepoint to the initial transmittance and assuming that the quantity of scattered light remained constant for all concentrations of H in WO_3:

$$\alpha(x, y, t) = T(x, y, t = 0) - T(x, y, t) \tag{1}$$

In Equation 1, T is the measured transmittance and α is the corresponding absorbance at pixel position (x, y) and time t. As the oxide films are reduced to bronzes, they shift to deep blue and absorb more of the incident light, where the first image of each experiment is of pure WO_3 and transmits the most light. In the formalism of Equation 1, $T(x, y, t = 0)$ will always be larger than $T(x, y, t)$ and will result in positive values of $\alpha(x, y, t)$. Extinction coefficients for various wavelengths of light interacting with H_xWO_3 have been determined for a range of hydrogen stoichiometries, x, for values < 0.4.[2] There is a monotonic increase in extinction coefficient with hydrogen content, which leads to a similar monotonic relationship between hydrogen content and absorbance. Therefore, although $\alpha(x, y, t)$ is not a rigorous measurement of absorbance, it is suitable for estimating relative hydrogen concentrations. We defined the edge of the moving front as the position of the leading edge of the absorbance profile at approximately half of the maximum observed value, which should correspond to a constant value of x in H_xWO_3.

2 Additional Materials Characterization

Samples were allowed to incubate at room temperature for at least three days after ion exchange, which allowed for full formation of the crystalline nanodisk morphology without the use of structure-directing agents. The tungstic acid solutions changed from clear yellow to opaque yellow in appearance over that timespan. Figure S2 shows SEM images the daily progression of product morphology. Each sample was prepared from the same batch of material and was calcined at 500 °C for one hour prior to imaging.

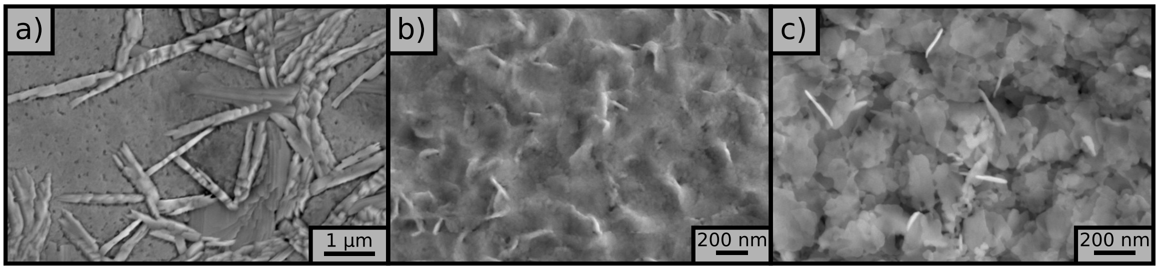

Figure S2: SEM images of tungsten trioxide thin films as a function of incubation time. Panel (a) shows the film morphology on the first day after ion exchange, which exhibits a distinct columnar structure interpenetrating a featureless background material. The Day 2 material in (b) shows the first indication of disk-like structure, with no remaining columnar shapes visible. Panel (c) confirms that on Day 3 the thin films achieve a consistent nanodisk morphology. There was no observed change in morphology after the third day of incubation.

X-Ray diffraction was performed alongside SEM to investigate any shifts in crystal structure that accompanied the development of the nanodisks. The results are shown in Figure S3. These data show clear increases in crystallinity and texture through the three days of incubation. As discussed in the main text, TEM imaging showed the zone-axis and crystal facets exposed on the plane-edge of the nanodisks to be in the (100)-family. XRD confirms a development of increased crystalline fraction in the (002) and (020) alongside the development of the disk shape.

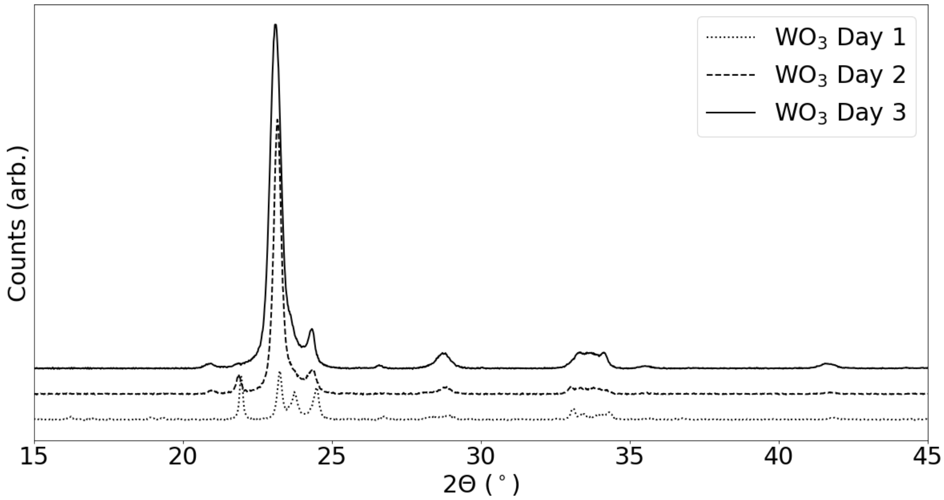

Figure S3: X-Ray spectra following the same temporal pattern as those shown above for SEM. A clear increase in diffraction intensity occurs alongside preferential texturing of the material in the (002) and (020) directions, consistent with the formation of nanodisks with predominantly (100)-family facets exposed on the plane face.

Although the disks were uniform at the micro-scale, we observed a considerable density of crystalline imperfection at the nano-scale. Figure S4 shows additional TEM images confirming observations made in SEM and illustrating these defects.

3 Effect of Restricting Proton Access

As noted in the main text, the observed migration rates of the coloration fronts were too fast to be attributed to proton diffusion in bulk tungsten trioxide when the WO_3 films were wetted with H_2SO_4 electrolyte. Hence, we argued that the electrolyte acts as proton source for bronze formation independent of the source of reducing equivalents. To further test this hypothesis, an electrochemical measurement was made on a sample identical to that in normal chronoamperometric experiments with the addition of a silicone layer on top of the pure WO_3. This was done to “shut-off” the electrolyte as a proton source, as illustrated in Figure S5.

Dow Sylgard 184 polydimethylsiloxane was employed as the silicone encapsulant, cured at 100 °C for 35 minutes at a ratio of 10:1 elastomer base to curing agent. A small gap was retained between the edge of the electrode and the beginning of the silicone layer. This allowed for direct comparison of electrolyte-exposed and electrolyte-isolated coloration fronts. The initial migration of protons occured rapidly, traversing the pure WO_3 area in seconds. Upon reaching the silicone covered WO_3, front progression was significantly slowed. Figure S6 shows a representative position vs. time curve collected for a silicone-covered region of a WO_3 film. The position of the silicone layer edge is taken as the zero position, and the time at which the front reached this edge (i.e. the time at which the front completely traversed the exposed WO_3 film) is taken as zero time. As can be seen, the front was found to move only $\sim$150 microns from the leading edge of the isolated film after 500 seconds. Furthermore, the shape of the position vs. time data are very well described by an equation of the form $x = At^{0.5}$, which suggests purely diffusional behavior. We further estimated a diffusion coefficient using $\delta = \sqrt{4Dt}$, resulting in an apparent diffusion coefficient of 1.30 x 10^{-7} cm^2/s.

The value above roughly agrees with the upper bound of diffusion coefficients that have been previously reported for proton diffusion in H_xWO_3.[3, 4, 5] However, it is considerably greater than that reported by Bohnke and Vuillemin for proton diffusion through dense WO_3 films also via optical measurements.[6, 7] One major difference between these measurements is the sample geometry. In Bohnke and Vuillemin’s case, diffusion rates were extracted from optical spectroscopy conducted normal to the direction of diffusion, which requires sampling the entire gradient of compositions (value of x in H_xWO_3). By contrast, our lateral measurements treat the H_xWO_3 propagation front at a single absorbance value corresponding to an intermediate state of hydrogenation. Hence, it is possible that the average rate of diffusion is in fact constrained by relatively slow transport at one particular composition (e.g., high or low H concentration). Another difference is that Bohnke and Vuillemin’s experiments were carried out on dense WOx films, while ours were on porous films of WO3 nanocrystals. In our case, it would be reasonable to conjecture that proton transport is predominantly occurring along WO_3 nanodisk surfaces, in which case it could be substantially enhanced by a hydrogen-bond network at the oxide/electrolyte interface.

4 Mechanistic Formulation

The results of this study indicate that in the presence of a proton-conducting medium, H-intercalation and H-spillover in WO_3 proceed by the same mechanism involving proton and electron transfer, wherein the proton and electron need not originate from the same source. However, it remains unclear whether the temporal course of the reaction involves sequential or concurrent proton and electron transfer steps. Figure S7 compiles a family of candidate reaction mechanisms comprising a series of electron tranfer (ET), proton transfer, (PT) or proton-coupled electron transfer (PCET) steps first to a surface WO_3 site and then into the bulk of the WO_3 crystal.[8] We speculate that the predominant mechanism in this system involves two concurrent PCET steps—corresponding to the diagonal path through this diagram—due to the delocalization of electrons in the WO_3 conduction band, which could facilitate rapid charge compensation of protons as they adsorb and intercalate. Additional experiments (e.g., pH dependence, kinetic isotope effect, etc.) would be warranted to further distinguish between these mechanisms.

References

[1] Abraham Wolcott, Tev R Kuykendall, Wei Chen, Shaowei Chen, and Jin Z Zhang. Synthesis and characterization of ultrathin wo3 nanodisks utilizing long-chain poly (ethylene glycol). *The Journal of Physical Chemistry B*, 110(50):25288–25296, 2006.

[2] K Bange. Colouration of tungsten oxide films: A model for optically active coatings. *Solar Energy Materials and Solar Cells*, 58(1):1, 1999.

[3] Paul A Sermon and Geoffrey C Bond. Studies of hydrogen spillover. part 1.—study of the rate, extent and products of hydrogen spillover from platinum to the trioxides of tungsten and molybdenum. *Journal of the Chemical Society, Faraday Transactions 1: Physical Chemistry in Condensed Phases*, 72:730–744, 1976.

[4] M Stanley Whittingham. Hydrogen motion in oxides: from insulators to bronzes. *Solid State Ionics*, 168(3-4):255–263, 2004.

[5] YM Li, M Hibino, M Miyayania, and T Kudo. Proton conductivity of tungsten trioxide hydrates at intermediate temperature. *Solid State Ionics*, 134(3-4):271–279, 2000.

[6] O Bohnke, M Rezrazi, B Vuillemin, Cl Bohnké, PA Gillet, and C Rousselot. “in situ” optical and electrochemical characterization of electrochromic phenomena into tungsten trioxide thin films. *Solar energy materials and solar cells*, 25(3-4):361–374, 1992.

[7] B Vuillemin and O Bohnke. Kinetics study and modelling of the electrochromic phenomenon in amorphous tungsten trioxide thin films in acid and lithium electrolytes. *Solid State Ionics*, 68(3-4):257–267, 1994.

[8] James M Mayer. Proton-coupled electron transfer: a reaction chemist’s view. *Annu. Rev. Phys. Chem.*, 55:363–390, 2004.

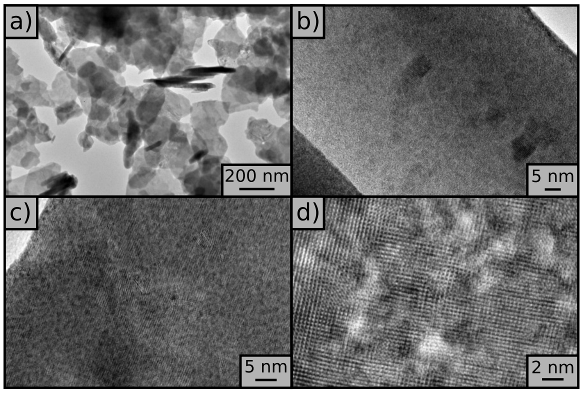

Figure S4: TEM micrographs showing key characteristics of the as-synthesized material at several length scales. Panel (a) shows a grouping of disks, confirming the micro-scale structure and the dimensions observed in SEM. Panels (b) and (c) show regions of the plane face of the nanodisks where various grain sizes and multiple defects are evident. Panel (d) shows lattice fringes indicative of numerous stacking faults and other crystallographic irregularities.

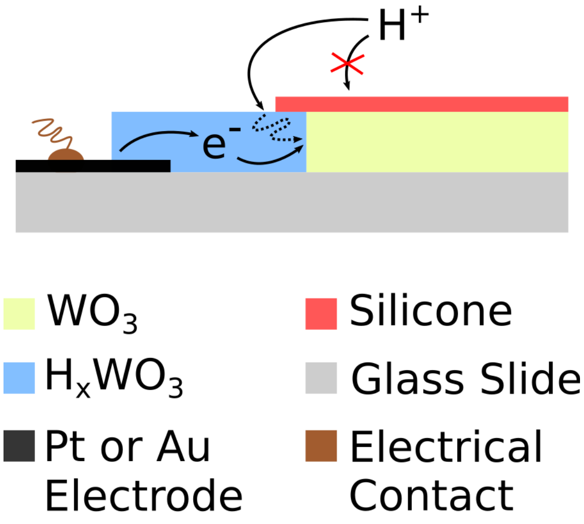

Figure S5: Schematic describing the function of the additional silicone elastomer film to eliminate direct proton transfer to the WO_3 film. Restricting access to the electrolyte-sourced protons would require bronze formation to occur by sourcing protons from through the already reduced bronze; in other words, the system would be dependent on proton and electron diffusion through the H_xWO_3 film. This process is represented by the dotted arrow and is expected to be slower than the incorporation of protons from the local electrolyte.

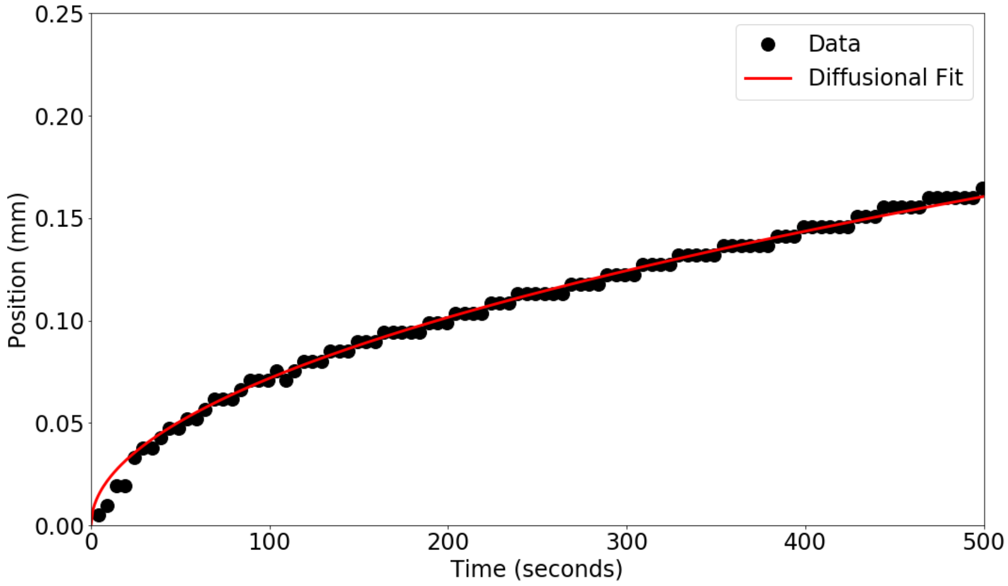

Figure S6: Position vs. time data for lateral propagation of a H_xWO_3 diffusion front using the experimental configuration in Figure S5. The linear fit corresponds to the predicted position vs. time data for a diffusion coefficient of 1.3x10^{-7} cm^2/s

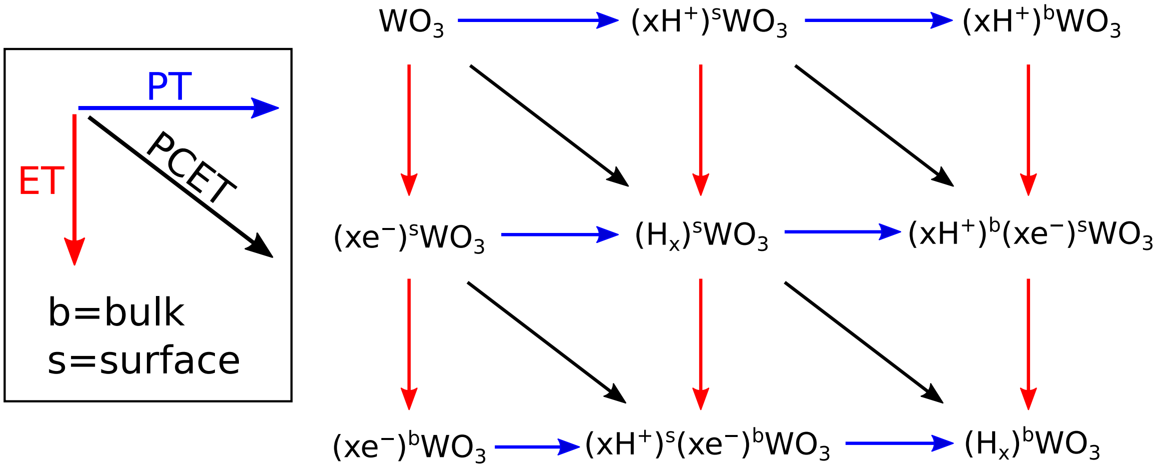

Figure S7: Compiled mechanistic pathways for H uptake in WO_3 according to a series of square schemes involving either sequential electron and proton transfers or concerted proton-coupled electron transfers first to the surface of a WO_3 crystallite and then into the bulk crystal lattice.